

Fast Horizon Approximation: Impacts on Integrated Photovoltaic Irradiation Simulations

Evgenii Sovetkin,* Andreas Gerber, and Bart E. Pieters

In applications that utilize detailed solar resource assessments with high-resolution topography data, calculating the topographic horizon is critical for accurate shading calculations. In particular, the horizon calculation significantly influences the time needed to model solar irradiation in integrated photovoltaic applications. The new approximate horizon algorithm was developed to balance accuracy and computation time. This study evaluates the algorithm's performance in modeling vehicle- and building-integrated photovoltaics, considering the impact of surface orientation and elevation. It is demonstrated that the proposed horizon algorithm achieves the same level of accuracy four times faster than previously known approaches for vehicle-integrated applications. Moreover, for building-integrated applications, the proposed approach performs better at elevations higher than 10 m on facades and roofs. Finally, the impact of maximum sampling distance on irradiation for high- and low-resolutions topography is studied.

1. Introduction

Analyzing different integrated photovoltaic (PV) systems is a detailed process that involves careful simulations. Shadows created by surrounding structures and vegetation significantly impact such PV systems. Calculating its impact can be time-consuming, especially when modeling integrated PV systems in urban areas.

The dynamic nature of vehicle-integrated PV (VIPV) systems results in significant performance variations depending on the vehicle's geographical position. This means researchers must conduct specific VIPV-related irradiance simulations for each location. Furthermore, the distribution of sunlight on a vehicle is significantly influenced by its location and the type of road.^[1] Shading from the terrain has a considerable impact on reducing the efficiency of the VIPV system,^[2–5] leading to an average loss of 40% on the roof surfaces.^[6] Similar challenges are encountered in other integrated photovoltaic applications, such as

road-integrated PV (RIPV) and building-integrated PV (BIPV).^[7–9] Given the substantial variation in terrain, simulation algorithms for integrated PV applications must be well-optimized to evaluate shading effects on a large scale. Therefore, a thorough analysis of high-resolution topography data is essential. The accuracy of sunlight modeling is critical in predicting system output and optimizing the design and size of PV systems.

The estimation of the horizon significantly affects the time required for simulating irradiance with high-resolution topography data.^[1,5,8,10] Previous methods for determining the horizon have involved approximations and sampling the topography in a finite number of directions.^[11,12]

Many software packages have adopted this approach. However, our recent work^[13] introduced a new algorithm that uses quasirandom sequences for sampling. Our method achieves higher accuracy with fewer sampling points, resulting in faster computation.


Our previous work^[13] delved into the technical aspects of the algorithm, such as memory performance and scalability. In contrast, this article focuses on the practical implications of the horizon algorithm in the context of integrated PV systems. Here, we evaluate the algorithm's performance and accuracy in real-world VIPV and BIPV irradiation simulation applications, shedding light on its practical utility. We also address the question of the maximum sampled topography distance and its impact on the horizon accuracy. Our findings underscore the importance of this parameter, as insufficient topography sampling can lead to a significant overestimation in irradiation for specific locations. As a result, we provide concrete recommendations on sampling low- and high-resolution topographies. Finally, we study the impact of the Earth's curvature correction on irradiation modeling.

The article is structured as follows. Section 2 comprehensively reviews the data sources used in our study. Section 3 focuses on the horizon algorithm, discussing its implementation and evaluation methodology. Finally, Section 4 evaluates algorithm performance for vehicle- and building-integrated irradiation simulation and studies the impact of the maximum topography sampling distance.

2. Data Sources

In our research, we use various data sources, such as high- and low-resolution topography data, satellite-based irradiation data, OpenStreetMap (OSM) data for street locations, building model

E. Sovetkin, A. Gerber, B. E. Pieters
IMD-3 Photovoltaics
Forschungszentrum Jülich
52425 Jülich, Germany
E-mail: e.sovetkin@fz-juelich.de

 The ORCID identification number(s) for the author(s) of this article can be found under <https://doi.org/10.1002/solr.202400474>.

© 2024 The Author(s). Solar RRL published by Wiley-VCH GmbH. This is an open access article under the terms of the Creative Commons Attribution License, which permits use, distribution and reproduction in any medium, provided the original work is properly cited.

DOI: 10.1002/solr.202400474

data (GML, level-of-detail [LoD-2]), and a 3D model of commercial vehicle. Part of our study focuses on specific streets and buildings in the state of North Rhine-Westphalia in Germany. In contrast, another part uses randomly sampled topography across Europe and the USA.

We use light detection and ranging (LiDAR)-derived rasters for high-resolution topography data. Specifically, we utilized $0.5 \times 0.5 \text{ m}^2 \text{ pixel}^{-1}$ digital surface model (DSM) data obtained by selecting the maximum elevation of all LiDAR cloud points in every $0.5 \times 0.5 \text{ m}^2$ region. This dataset covers a vast area of $300\,000 \text{ km}^2$ in Europe and the USA. The European subset spans $100\,000 \text{ km}^2$, encompassing areas in France, Germany, Luxembourg, and Spain. The USA data covers $200\,000 \text{ km}^2$ and includes areas from New York, New Jersey, Nevada, Arizona, South Dakota, Alaska, Florida, Georgia, and Hawai'i states. Figure 9 visually represents the LiDAR data locations, with red dots indicating a random sample of 5313 points. Table 1 details the specific data sources we have utilized in our study.

To study the effects of general topography and the Earth's curvature on irradiation, we use low-resolution satellite-measured topography data, Advanced Spaceborne Thermal Emission, and Reflection Radiometer (ASTER).^[14] It has a coarse spatial resolution of $30 \times 30 \text{ m}^2 \text{ pixel}^{-1}$. The satellite-based topography data does not capture any building or vegetation but provides a generic topography outlook.

In addition to the topography data, we incorporate historical atmosphere irradiation data from Copernicus over 11 years.^[15] This service provides ground-level global horizontal (GHI) and diffuse horizontal (DHI) irradiance data for Europe and Africa, taking into account cloud coverage. The data, which has a low temporal and spatial resolution (one observation per 10 min and $5 \times 5 \text{ km}^2$ area), is used as input for the Perez All-Weather Sky model.^[16] This model allows us to simulate irradiation in different sections of the sky. Furthermore, we can model yearly irradiation for specific locations by integrating the sky over time. Figure 1 depicts the integrated sky used throughout simulations in this article.

The performance of the horizon algorithm matters most for complex environment topography and large-scale simulations. Therefore, we study the impact of the horizon approximation on VIPV and BIPV applications, where we model irradiation on the surface of a car placed on random locations and a sample of buildings. For the vehicle model, we use the surface from ref. [1], where the car is modeled using a sample of points containing 3D coordinates and orientation of the normal vector to

Table 1. Publicly available LiDAR data sources.

Country	Citation
USA	[44]
Germany, NRW	[45]
Germany, Berlin	[46]
Luxembourg	[47]
Switzerland	[48]
France	[49]
Spain	[50]

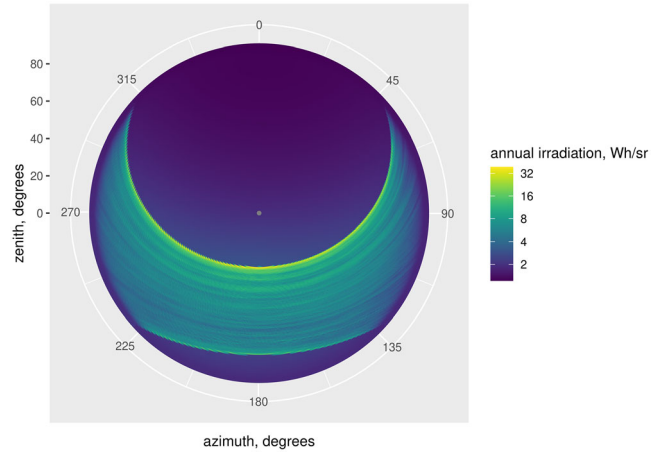


Figure 1. 11 years integrated sky for Groningen, the Netherlands. Each point color shows average over 11 years annual irradiation in Wh/sr.

the surface. The vehicle is placed on random streets, and sampling is performed using OSM data.^[17,18] For building surfaces, we use GML-derived data from the state of North-Rhine Westphalia.^[19] We use LoD2 data, which describes buildings with correct facades and roof shapes but lacks details on windows or surface material. Similarly to vehicle shapes, building surfaces are represented as points with normal vectors.

3. Approach

The horizon separates the visible sky from the ground for a given observer location and plays a pivotal role in irradiation modeling and computing PV solar potential. Horizon profile is used as input in numerous PV simulation tools, including but not limited to PVGIS,^[20] PVlib,^[21] PVSOL,^[22] and PVsyst.^[23] The horizon computation from topography data is implemented in several software packages, such as GRASS GIS,^[24] ArcGIS,^[25] SAGA GIS,^[26] HorizonScanner,^[27] HORAYZON,^[28] and simple sky dome projector (SSDP).^[29]

Horizon computation requires searching for parts of the sky covered by a given topography. For large volumes of data, one needs to analyze topography elevation and the corresponding distances to an observer. The topography model we work with is described by a function $T: \mathbb{R}^2 \rightarrow \mathbb{R}$, $(x, y) \mapsto z$, where (x, y) are geographical coordinates in some geographical coordinate system, and z defines the height of the topography. The regularly sampled DSM with a finite number of pixels is given by a raster image, where sampling is defined by the starting geographical coordinate $(x_0, y_0) \in \mathbb{R}^2$, image resolution $WH > 0$, and sampling step size is dx . For instance, the raster we work with has a pixel size of $0.5 \times 0.5 \text{ m}^2 \text{ pixel}^{-1}$. Hence, the corresponding step size equals $dx = 0.5 \text{ m}$. We denote such rasters as matrices

$$\mathbf{T} := \{T(x_0 + (i-1)dx, y_0 + (j-1)dy)\}_{i \in 1:W, j \in 1:H} \in \mathbb{R}^{W \times H}, \quad (1)$$

$W, H \in \mathbb{N}$

For the horizon, we consider the topography representation in polar coordinates at a given observer location $(x, y) \in \mathbb{R}^2$. For a

$r > 0, \phi \in [0, 2\pi)$, let

$$\xi_0(r, \phi) = \xi_{0, (x, y)}(r, \phi) := \max(T(x + r \cos(\phi), \gamma + r \sin(\phi)) - T(x, \gamma) - o - E(r), 0) \quad (2)$$

where $o \geq 0$ is the offset or elevation of the observer away from the ground, and $E(r)$ is the Earth curvature correction term:

$$E(r) := R_{\text{Earth}}(1 - \cos(r/R_{\text{Earth}})), \quad R_{\text{Earth}} = 6378.137 \text{ km}, \quad r > 0 \quad (3)$$

The horizon is then defined as a function $h:[0, 2\pi) \rightarrow [0, \pi/2]$

$$h(\phi) := \max_{r>0} \arctan\left(\frac{\xi_0(r, \phi)}{r}\right) \quad (4)$$

Here, we assume that the horizon takes only non-negative values, that is, $h(\phi) \in [0, \pi/2]$, because we ignore all sectors of lower topography (note \max in (2)). We use the lower hemisphere to model the reflection from the ground (albedo effect).

Algorithm 1 outlines the steps for computing (4) using the given topography raster \mathbf{T} and sampling strategy S . In Step 1, the inputs include a set of observer locations expressed in pixel coordinates (k, l) within raster \mathbf{T} and the elevation o in meters. The horizon is evaluated at a fixed number of azimuth directions defined by the set Φ . In our implementation, we utilize the finest set Φ with equidistant points in the interval $[0, 2\pi)$, where the distance between points is determined by the azimuthal range of a corner pixel observed from the opposite corner of the raster.

The sampling strategy is defined as a set of polar coordinates $S := \{r, \phi\}$ and determines where the topography pixels are sampled (see `PIXEL_SAMPLESET` procedure in Steps 4–11). The `PIXEL_SAMPLESET` also precomputes the azimuth angle range for each sampling point (see `arange` procedure in Steps 2–3). Due to the computation performance consideration in Step 9, we use the following approximation of the Earth correction term

$$E(r) := R_{\text{Earth}}(1 - \cos(r/R_{\text{Earth}})) \approx \frac{r^2}{2R_{\text{Earth}}}, \quad 0 < r \ll R_{\text{Earth}} \quad (5)$$

where the absolute approximation error is within 1.6 cm in a 100 km radius and 26 cm in a 200 km radius. Due to the division by r in Step 16, the approximation errors are negligible for any distances considered.

The horizon is computed for all observer locations in the loop in Step 20 of Algorithm 1. The HORIZON procedure iterates over all topography sampling points in Steps 12–18. For each sampling point, the affected horizon elements are updated for all angles in the set $\Phi \cap [\phi_0, \phi_1]$ (see Step 16).

Algorithm 1 gives not a single algorithm but an algorithm family, obtained by varying the sampling strategy S . For example, the proposed approximate horizon algorithm in literature^[11,12] is given by the sampling strategy depicted in Figure 1, left. We refer to this sampling strategy as “Rays,” with the main idea of which is to divide the horizon into several sectors and, in each direction, determine the maximum angular elevation of the horizon by sampling terrain points on the centerline. The optimal number of rays is discussed in literature,^[30] with 32 rays being commonly

Algorithm 1. Approximate horizon algorithm using topography sampling.^[13]

1: Input:

- Topography $\mathbf{T} \in \mathbb{R}^{W \times H}$ with the pixel step dx.
- Topography sampling strategy S .
- Set of observer locations and heights $L := \{(k, l, o)\}$, where (k, l) corresponds to the pixel coordinates of the topography \mathbf{T} and $o > 0$ is the observer height (offset away from the ground).
- Horizon azimuth angle set $\Phi \subset [0, 2\pi)$.
- $R_{\text{Earth}} \leftarrow 6378137\text{m}$

2: **procedure** ARANGE (m, n)

3: **return** (ϕ_0, ϕ_1) azimuthal range occupied by the pixel (m,n) viewed from $(0,0)$

4: **procedure** PIXEL_SAMPLESET(S)

5: $P_S \leftarrow \{\}$ ▷ signed pixel coordinates corresponding to S

6: **for** $(r, \phi) \in S$ **do**

7: $m \leftarrow [\cos(\phi)r/dx], \quad n \leftarrow [\sin(\phi)r/dx]$

8: $(\phi_0, \phi_1) \leftarrow \text{arange}(m, n)$

9: $E \leftarrow r^2 / (2R_{\text{Earth}})$ ▷ Earth curvature correction term, see (5)

$$10: \quad P_S \leftarrow P_S \cup \{(m, n, (dx\sqrt{m^2 + n^2})^{-1}, \phi_0, \phi_1, E)\}$$

```

11: return  $P_S$ 

```

12: **procedure** HORIZON (k, l, o)

13: $\forall \phi \in \Phi: h(\phi) \leftarrow 0$

14: **for** $(m, n, x, \phi_0, \phi_1, E) \in P_S$ **do**

```

15:   if  $m + k \notin 1:W$  or  $n + l \notin 1:H$  then next

```

16: $\forall \phi \in \Phi \cap [\phi_0, \phi_1] : h(\phi) := \max(h(\phi), x(\mathbf{T}_{m+k, n+l} - \mathbf{T}_{k,l} - o - E))$

17: $\forall \phi \in \Phi: h(\phi) \leftarrow \arctan h(\phi)$

```

18:   return  $h$ 

```

19: $P_S \leftarrow \text{pixel_sampleset}(S)$

20: **for** $(k, l, o) \in L$ **do** ▷ loop iterations are done in parallel

21: $h_{k,l,o} \leftarrow \text{horizon}(k, l, o)$ 22: **Output:** $\forall (k, l, o) \in L: h_{k,l,o}(\phi) \in [0, \pi/2), \quad \phi \in \Phi.$

adopted as a default option.^[31] This method, while less precise than the exact horizon computation, significantly reduces the computation time without compromising the overall accuracy of the results.

The exact horizon algorithm requires verification of every pixel in the given topography. The corresponding topography sampling set P_S contains exactly WH points and hence involves significantly longer computation times. For comparing sampling algorithms, it is beneficial to consider the restricted sampling set $P_{S_{\text{disk},R}}$, where the topography is sampled for all pixels within the distance R from the observer. This way, the horizon’s errors are not influenced by points outside the disk.

Our previous work has shown that “Rays” sampling is not the most efficient strategy.^[13] We have experimented with several sampling strategies, S , and have found that the best-performing strategy estimates the distribution of argmax in (4), derived from computations based on a large sample of topography data covering 300 000 km² in Europe and the USA. This optimal sampling

strategy, depicted in **Figure 2**, right, turns out to be faster and more precise than the “Rays” sampling strategy.^[13]

We attribute those improvements to random sampling in azimuth directions. In ref. [13], we established that the type of randomness also matters. We use Sobol’s quasirandom sequences as an inducing sequence for the topography sampling strategy S . In contrast, the algorithm’s performance degrades by 18% when independent and identically distributed random sampling is used instead.

Several technical details must be considered when implementing Algorithm 1, discussed in detail in ref. [13]. For example, location ordering influences the CPU cache misses, introducing memory bandwidth bottlenecks. Similar implementation optimizations also appear in the literature.^[10] uses vectorized tensor arithmetic to analyze topography and identify shaded areas.^[28] uses the high-performance ray-tracing library to improve computation speed for the sky view factor. However, no matter how Algorithm 1 is implemented, its running time scales linearly with the number of sampling points P_S ,^[13] and therefore, sampling strategy is the primary factor of algorithm performance.

This article focuses on PV-related aspects of approximate horizon computation. It evaluates the performance and accuracy of several algorithms on typical integrated PV applications such as VIPV and BIPV by simulating irradiation on vehicle bodies and building facades for different sampling strategies (see methodology in Section 3.1). There, we consider roads and buildings within North-Rhine Westphalia in Germany. Section 3.2 considers a more global outlook with topography sampled throughout the available data (see Figure 9), where we study the effects of the maximum distance from the observer ($dx\sqrt{m^2 + n^2}$ in Line 10 in Algorithm 1) on the algorithm’s accuracy. The latter allows a further decrease in the number of points in P_S , improving the overall computation times.

3.1. Algorithm Evaluation for VIPV and BIPV Applications

The performance of the horizon algorithm is most important for complex environmental topography and large-scale simulations. Therefore, we are studying the impact of the horizon approximation on VIPV and BIPV irradiation modeling applications. To accomplish this, we are comparing irradiation modeling on vehicle and building surfaces using both approximate and precise horizon algorithms.

Figure 3 shows two examples of a vehicle and a building surface. In both cases, the surfaces are represented as a set of 5D points describing the 3D coordinate and the direction of the surface’s normal vector. In our simulations, we use a reduced set of surface locations containing 10% of all points depicted in Figure 3.

For sampling locations, we use fixed anchor points in various towns in the North-Rhine Westphalia state in Germany (see **Table 2**). A rectangular area is selected around each anchor location with a rectangle side of 4 km. In every area, we sample 200 random buildings and 500 places on roads. The vehicles are placed on random road locations extracted from OSM data.^[17] Both building and vehicle locations are sampled at least 250 m from the considered area boundary. Therefore, the locations are distributed within an area of 12.25 km².

Our main objective in VIPV and BIPV simulations is to compare the accuracy of different horizon approximation methods. We conduct annual irradiation simulations using both approximate and precise horizon estimation methods. Our irradiation modeling is carried out in SSDP,^[29] where the modeled sky is projected onto the oriented plane surface, considering its orientation and angular-dependent reflection coefficients. We use the same integrated Perez All-Weather sky model shown in Figure 1 for all simulated locations, ensuring that irradiation simulations

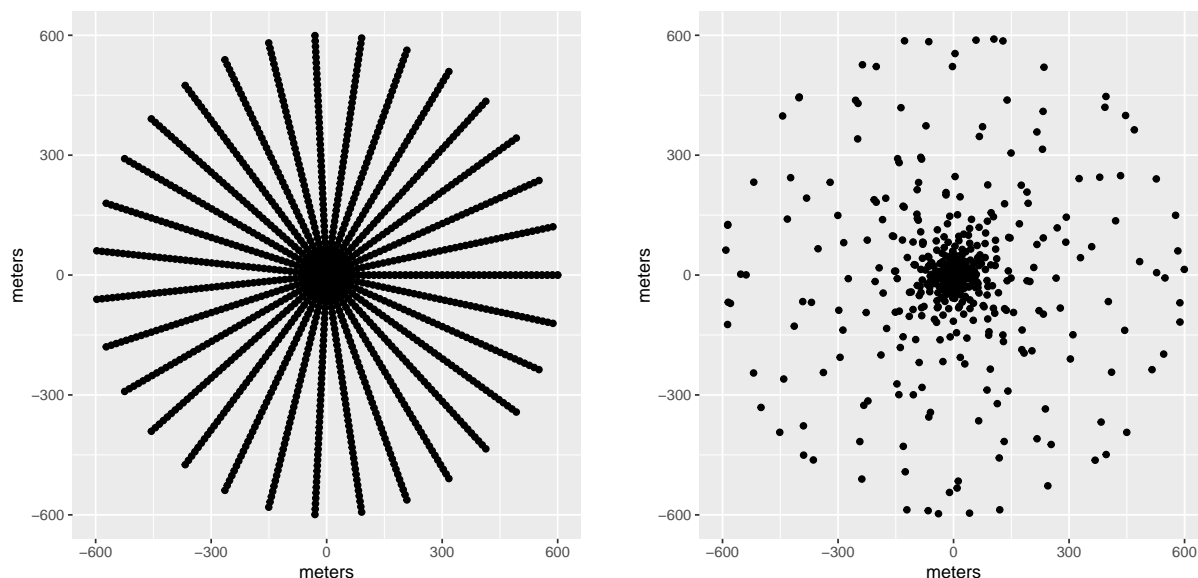


Figure 2. Comparison of the old topography sampling strategy (left, with 32 rays) and the new proposed sampling strategy (right). Each point indicates the topography sampling point relative to the observer at the origin (axes’ units in meters). Both figures contain 1440 points and sample topography at the maximum distance of 600 m. Axes units: meters.

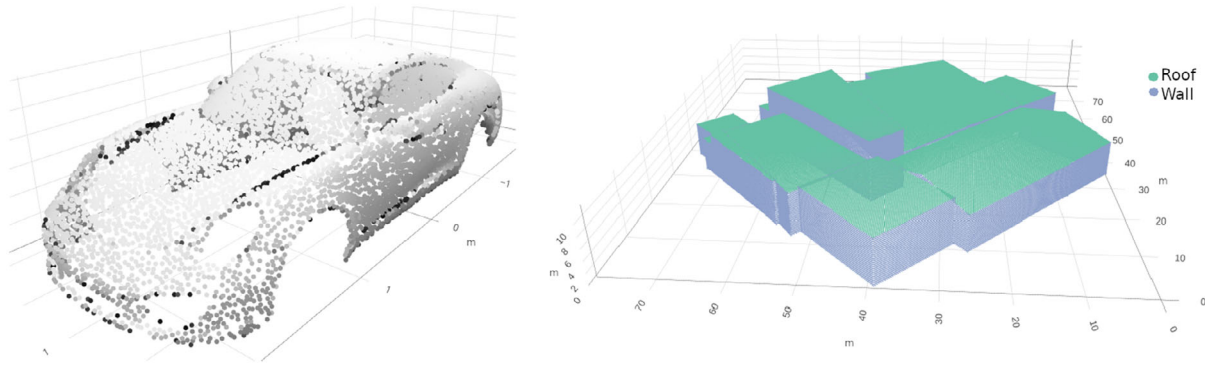


Figure 3. Left: vehicle surface points (same vehicle shape used in ref. [1]). Right: the cafeteria building complex in the Jülich Research Center campus. Green indicates the roof, and blue indicates wall surfaces. Axes units: meters.

Table 2. Locations of anchor points, the number of building parts, and length of roads within the considered rectangular area of 12.25 km² around the anchor point.

Location	Latitude	Longitude	# of buildings	Road length [km]
Düsseldorf	51.2162	6.8123	31 604	511
Köln, left bank	50.9340	6.9495	35 644	536
Köln, right bank	50.9320	7.0464	17 468	414
Wuppertal	51.2607	7.1728	27 380	434
Dortmund	51.5171	7.4824	24 179	662
Münster	51.9335	7.6345	14 759	407
Lindlar	51.0195	7.3727	7721	174
Wewer	51.6896	8.6919	6393	181
Winterberg	51.1891	8.5120	3970	251
Schmidt, Eifel	50.65084	6.41324	3658	138
Jülich	50.90455	6.41125	2671	166

can be compared across locations and are not reliant on the sun's trajectory.

In addition, we standardize the irradiation and express it as a relative quantity. Specifically, we calculate a ratio of irradiation with and without the influence of topography. This normalization always results in values between 0 and 1, and one minus that quantity can be interpreted as the percentage of losses attributed to the shading from topography. It's important to note that relative irradiation does not account for transposition losses and only describes irradiation losses caused by shading from topography. This metric, called "relative notopo irradiation" in ref. [1], is useful for averaging irradiation on different surface orientations.

To evaluate the performance of various algorithms, we will assess the root mean square error (RMSE) for relative irradiation, which will be calculated using the approximate and precise horizon algorithms. The precise horizon will be determined using the $S_{\text{disk},R}$ topography sampling strategy. We will maintain a fixed maximum topography sampling distance of $R = 250$ throughout our simulations. The RMSE will be averaged across different observer locations and surface orientations.

In general, a sampling strategy can be generated in the following way. For $n \in \mathbb{N}$, let $U_n := \{(x_i, y_i) \in [0, 1]^d | i \in 1:n\}$ be an inducing sequence. We select U_n as a quasirandom Sobol sequence; however, it can be chosen as an independent and identically distributed sample of uniformly distributed random variables in $[0, 1]^2$. For a monotonically increasing function $F: [0, 1] \rightarrow [0, \infty)$, we apply the following transformation to U_n to obtain the sampling strategy

$$S := \{(F(x_i), 2\pi y_i) | (x_i, y_i) \in U_n\} \quad (6)$$

where the coordinates of S are polar coordinates of the sampled topography locations, where $F(x_i)$ is the polar radius measured in meters, and $2\pi y_i$ is the polar angle measured in radians. Function F can be interpreted as an inverse cumulative distribution function of some non-negative random variable, providing a way to generate a variety of sampling strategies by selecting different distributions.

Table 3 lists the sampling strategies used in simulations of this article. For a comprehensive study of various topography sampling strategies, we refer the reader to ref. [13].

3.2. Maximum Distance of Sampled Topography

In the realm of irradiance simulations, a fundamental question arises: how far from the observer should one examine the

Table 3. Definitions of the sampling strategies.

Sampling strategy	Description
"Precise"	$S_{\text{disk},R}$ is all topography pixels within the distance R from the observer.
"IID"	F is LIDAR_0 estimated from ref. [13]. U_n is independent uniformly distributed in $[0, 1]^2$.
"Rays"	Every pixel on the ray up to 250 m distance from the observer (see Figure 2, left). Number of rays: 16, 32, 64, 128, 256.
"Sobol"	F is LIDAR_0 estimated from ref. [13]. U_n is Sobol low-discrepancy sequence.
"Weibull"	F_M^{Weibull} , see (9) in Section 3.2.

elevation of the high-resolution topography? The further the topography is sampled, the more significant portion of the sky it may cover, potentially reducing the amount of light reaching the observer. Consequently, a shorter distance might lead to over-estimating the simulated irradiance. Typically, an arbitrary distance is selected, such as 100,^[32] 250,^[5,33,34] 500,^[1,13,35] 1000,^[9,36] and 1500 m.^[31] These distances are often chosen based on the data's resolution and the area's size being studied. However, this crucial information is frequently omitted in the literature,^[37–42] often due to the absence of software documentation or open-source code. To our knowledge, no study has looked into how a specific choice influences irradiation in various locations.

Results obtained in ref. [13] suggest that, for the high-resolution LiDAR data, the maximum value in (4) in more than 45% of cases is achieved further away than 100 m. However, this does not directly imply that objects further away strongly impact the resulting irradiation. To address this, we perform irradiation simulations for a large random sample of locations throughout the available topography data, encompassing different types of terrain and climate. We sample topography with varying distances using a parametric family of sampling strategies S in Algorithm 1 to evaluate the effect on the relative irradiation of an observer surface.

We use a family of truncated Weibull distributions to evaluate the effect of the maximum distance from an observer. The particular choice of the Weibull distribution family is due to its shape resembling the shape of the estimated optimal distribution obtained from sampling topography data (see Figure 2, right). By choosing the support of the truncated distribution, we can modify the maximum sample topography relative to the observer. The parametric family's choice allows for isolating effects of the maximum sampling distance and ignoring any effects attributed to the shape of the sampled distribution. Furthermore, we control the number of sampled points, allowing us to ensure that the number of sampled points at each radius is the same for different sampling strategies.

Formally, given the scale $\lambda > 0$ and shape $k > 0$ parameters, the Weibull cumulative distribution function is given by

$$W(x; \lambda, k) := (1 - e^{-(x/\lambda)^k}), \quad x \geq 0 \quad (7)$$

Let M be the maximum sampled distance; then the truncated Weibull distribution on the interval $[0, M]$ is given by the following cumulative distribution function.

$$W_M(x; \lambda, k) := \frac{W(x; \lambda, k)}{W(M; \lambda, k)}, \quad x \in [0, M] \quad (8)$$

Our topography sampling strategy is defined by inverting the cumulative distribution function W_M

$$F_M^{\text{Weibull}}(x) := \lambda(-\ln(1 - xW(M; \lambda, k)))^{1/k}, \quad x \in [0, 1] \quad (9)$$

where we chose $\lambda = 100$ and $k = 0.3$. Table 4 shows the number of sampled points for different values of M , which ensures a fixed number of points sampled within a given radius. Figure 4 demonstrates this by depicting the sampled locations, with different azimuthal sectors visualizing distribution for different M . The density of points shown in Table 4 between 1600 and 1900 m

Table 4. Values of M (meters) determining the support of the truncated Weibull distribution and the corresponding sample sizes.

M [m]	Sampled points
100	126 424
200	141 608
300	150 204
400	156 069
500	160 446
600	163 890
800	169 053
1000	172 804
1300	176 903
1600	179 895
1900	182 196

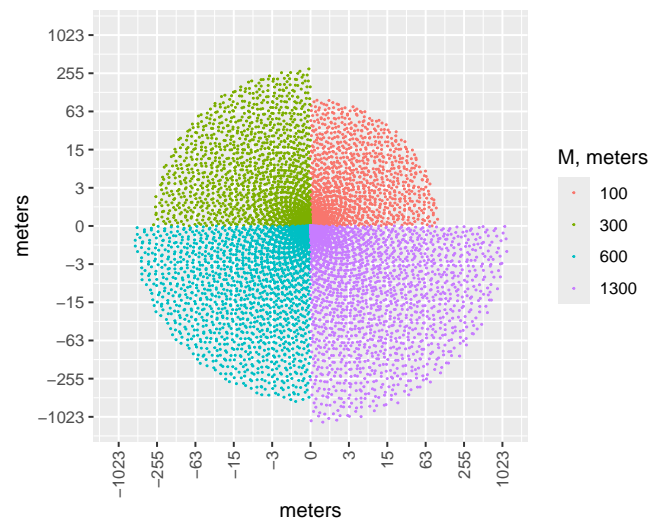


Figure 4. Visualization of the sampled locations for different values of parameter M (meters). The sampling sizes are reduced by 20 times for visualization purposes. Note the logarithmic scale of the axes. Axes units: meters.

from the observer is approximately one point for every $21 \times 21 \text{ m}^2$ area. Such density might not be sufficient for tall, narrow towers but good enough for tall buildings and hills further away.

4. Results

Our results compare the performance of the horizon algorithm by modeling irradiation on vehicle and building surfaces. The irradiation values depend on the elevation above the ground and the orientation of the observer's surface. Therefore, we study the impact of horizon approximation for VIPV (for a complex surface) and BIPV applications (for higher elevations above the ground), employing several sampling strategies S with varying numbers of sampling points.

4.1. VIPV: Sampling Strategy

Figure 5 presents the RMSE of relative irradiation using approximate and precise horizons for “IID,” “Sobol,” “Weibull,” and “Rays” sampling strategies (see Table 3 for definitions). We average errors using all vehicle surface points and all sampled vehicle locations. The y -axis, in a logarithmic scale, represents the RMSE between irradiation computed with precise and approximate horizon algorithms. The x -axis, also in a logarithmic scale, indicates the number of sampled topography points. The “Weibull” strategy is located between “IID” and “Sobol.” Notably, the “Rays” sampling strategy requires four times more topography sampling points to achieve the same accuracy levels as other strategies.

4.2. VIPV: Errors Distribution on the Body

It’s important to note that our study focuses on relative irradiation computed with and without the influence of the topography. Various factors, such as the type of road and the country, influence the actual irradiation of the vehicle’s body. For instance, the irradiation of vertical surfaces ranged between 30% and 60% of annual GHI.^[1] Assuming 1100 kWh m^{-2} , annual GHI irradiation in Germany translates to a range of $330\text{--}660 \text{ kWh m}^{-2}$. As shown in Figure 5, our results indicate that the “Rays” approximate horizon algorithm or insufficient sampling in other approaches may lead to significant overestimation of the irradiation. Figure 6 further illustrates the distribution of the RMSE of precise and “Rays” approach with 16 rays directions. While the vertical surfaces have more significant errors, it’s important to note that the overall orientation affects relative irradiation error within 1%.

4.3. BIPV: Approximation Errors on Roof and Facades

Height is another factor affecting irradiation. Typically, the higher the observer, the more sky is visible and hence the higher

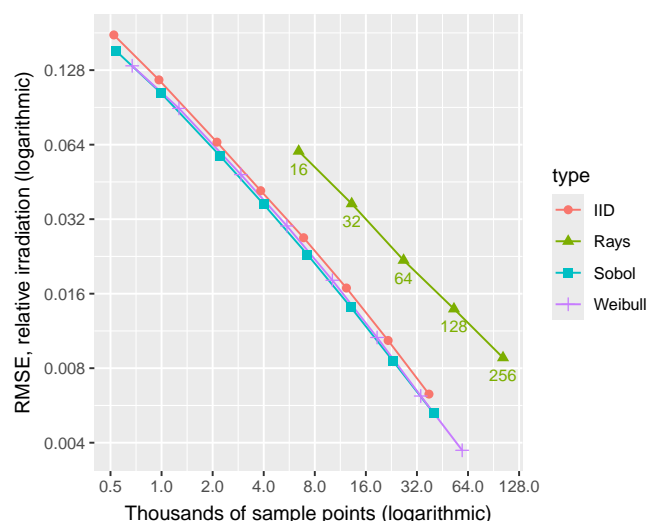


Figure 5. Comparison of RMSE averaged over the complete vehicle body. “Rays” sampling strategy corresponds to sampling with 16, 32, 64, 128, and 256 ray directions.

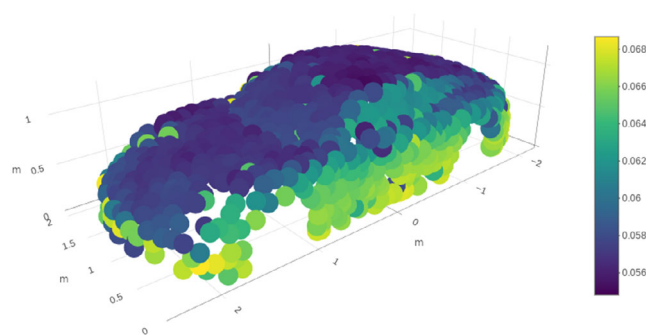


Figure 6. RMSE distribution on the vehicle body for “Rays” sampling strategy with 16 rays direction. Axes units: meters.

the irradiation. In our second experiment, we model irradiation on building surfaces with different sampling algorithms. Figure 7 depicts RMSE for wall and roof surfaces averaged over 900 000 walls (triangle dots) and 400 000 roofs (circle dots) randomly sampled points on buildings. Overall errors on wall surfaces are twice as significant as on roof surfaces, which is explained by the vertical orientation of the facades and the corresponding impact of shading. On observer elevations higher than 2 m, the difference between horizon sampling algorithms diminishes, with the “Rays” strategy with 256 rays outperforming other sampling strategies with a similar number of sampled points.

4.4. BIPV: Impact of Height

We explore further the impact of elevation in Figure 8. We compute RMSE (y -axis) for wall points for different levels above the ground (x -axis). Here, every dot is calculated by averaging errors over 60 000 locations. The errors gradually increase for all sampling strategies until they peak at 5 m above the ground. After

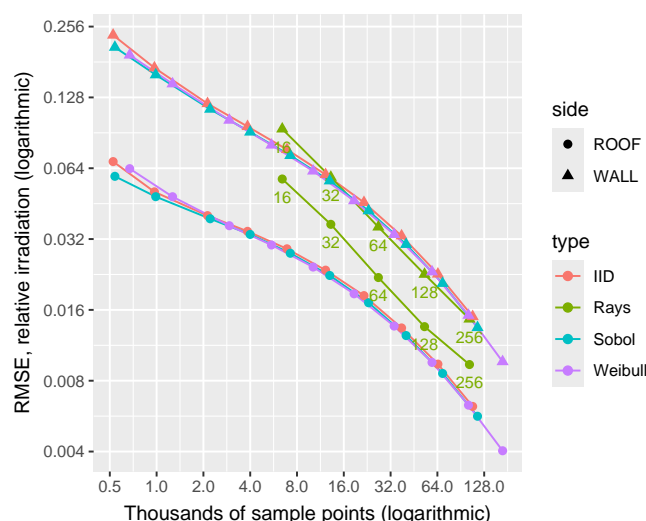


Figure 7. RMSE comparison for “Rays” and “Sobol” strategies between roof and walls. “Rays” sampling strategy corresponds to sampling with 16, 32, 64, 128, and 256 ray directions.

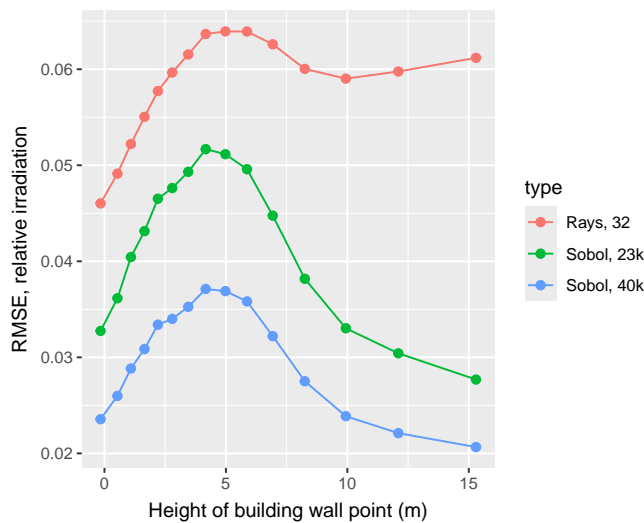


Figure 8. RMSE at different elevation on building walls.

that, the “Sobol” sampling strategy tends to decrease, and the “Rays” approach stays around at the peak level. We attribute this behavior to the fact that the “Sobol” strategy tends to sample point in all directions, whereas the “Rays” strategy has more significant gaps further away from the observer (see Figure 2, left). At higher elevations, the objects in those gaps start influencing the irradiation.

4.5. Maximum Sampling Distance

So far, we compared approximate horizon methods for a fixed maximum sampled distance of 250 m. To study the impact of the maximum sampled distance, we perform irradiation simulations for high- and low-resolution topography using the Weibull sampling strategy (see Section 3.2) to ensure the same number of points sampled at a given radius for each value M . We compute the averaged relative irradiation for a vertical observer plane oriented in eight directions for every 45° direction. The elevation of the observer is fixed at 1 m.

For high-resolution data, we generate a uniformly distributed set of 5313 anchor locations throughout the available topography of $300\,000\text{ km}^2$ (see Section 2). Around each anchor location, we sample an additional 10 000 equidistant points with 10 m between them. For the low-resolution data, we chose 2000 anchor locations distributed over central Europe, North India, Central Africa, and the east and west coasts of the USA. For each anchor location, an additional 4000 equidistant points were sampled.

Such a sampling approach allows a global search for locations where the maximum sampled topography distance influences the irradiation simulations. Generally, any horizon algorithm should perform well even with short maximum sampled topography distances on average. However, identifying critical regions allows describing locations where one must use more considerable distances.

To search for such critical regions, we look at the right tail of the error distribution. We compute the difference between relative irradiation calculated with the maximum topography sampled distance M and the corresponding value with a maximum distance of 1.9 km for LiDAR and 120 km for ASTER. Denote this difference

as $D_{M,1.9\text{km}}^{\text{LiDAR}}$ and $D_{M,120\text{km}}^{\text{ASTER}}$ for high- and low-resolution simulation respectively. The value of D can be directly interpreted as the amount by which irradiance is overestimated.

The red and blue dots in Figure 9 depict the sampled locations for the high-resolution data. The blue points indicate regions, where $D_{100\text{m},1.9\text{km}}^{\text{LiDAR}} > 0.1$. Typically, there is a high concentration of blue points in mountain regions (e.g., the Alps in Europe, and the Pacific Coast Ranges in the USA). Few blue points are located in flat terrain areas (Germany and South Florida). For $D_{100\text{m},1.9\text{km}}^{\text{LiDAR}}$, blue points occur throughout all considered locations, with higher concentrations around mountain areas. In contrast, the distribution of locations with $D_{600\text{m},1.9\text{km}}^{\text{LiDAR}} > 0.1$ is concentrated only around the mountain areas.

Figure 10 depicts the quantiles of the distribution of $D_{M,1.9\text{km}}^{\text{LiDAR}}$, $100\text{m} \leq M \leq 1.6\text{km}$ and $D_{M,120\text{km}}^{\text{ASTER}}$, $1\text{km} \leq M \leq 80\text{km}$ computed for all locations. The quantiles depicted offer a practical interpretation. For example, in 5% of all considered topography, the $M = 100\text{ m}$ -based horizon approximations yield overestimation of irradiation on vertical surfaces by more than 8%. For instance, in Germany, this translates to 140 kWh m^{-2} errors in annual irradiation.

The behavior of the distribution of $D_{M,1.9\text{km}}^{\text{LiDAR}}$ depends on the observer’s elevation. Generally, the higher the observer altitude, the higher the probability that objects further away affect the irradiation. The 95%-quantile of $D_{100\text{m},1.9\text{km}}^{\text{LiDAR}}$ at 2 m 0.09, whereas at 0 m it equals 0.06. The results above consider relative irradiation on a vertical surface positioned at 1 m above the ground. For horizontal surfaces, the impact of the topography is less; hence, the differences in relative irradiation are less dramatic than those on vertical surfaces. The 95%-quantile of $D_{100\text{m},1.9\text{km}}^{\text{LiDAR}}$ for horizontal surfaces ranges between 0.02 and 0.04 depending on the elevation.

Figure 11 depicts three examples with large values of $D_{100\text{m},1.9\text{km}}^{\text{LiDAR}}$. The red dots indicate all LiDAR locations with simulated irradiation, and the blue locations highlight the regions $D_{100\text{m},1.9\text{km}}^{\text{LiDAR}} > 0.1$. On the left side, the area of interest is in the middle of a meadow surrounded by the forest. The trees around the meadow are large enough to create a significant difference between computed irradiation. Similarly, the value D is large in the middle of a lake in the center figure. On the right part of Figure 11, the deviations are created by a large mountain. The interruption in the middle is due to a small village and trees, with the blue area inside agricultural fields. Generally, the object must be sufficiently large and close enough to an observer to have an impact on light and further away than $M = 100\text{ m}$ to affect the $D_{100\text{m},1.9\text{km}}^{\text{LiDAR}}$ value.

4.6. Effects of the Earth Curvature

Finally, we remark on the impact of the Earth curvature correction on the irradiation simulations. For high-resolution data and the maximum sampled distance of 1.9 km, the Earth curvature correction term is less than 28 cm. For low-resolution data and larger distances, the curvature effectively reduces the elevation of distant objects, yielding underestimated irradiation. Our low-resolution topography simulations, however, indicate that Earth curvature has effects smaller than 0.01 of relative irradiation in 99.5% of cases.

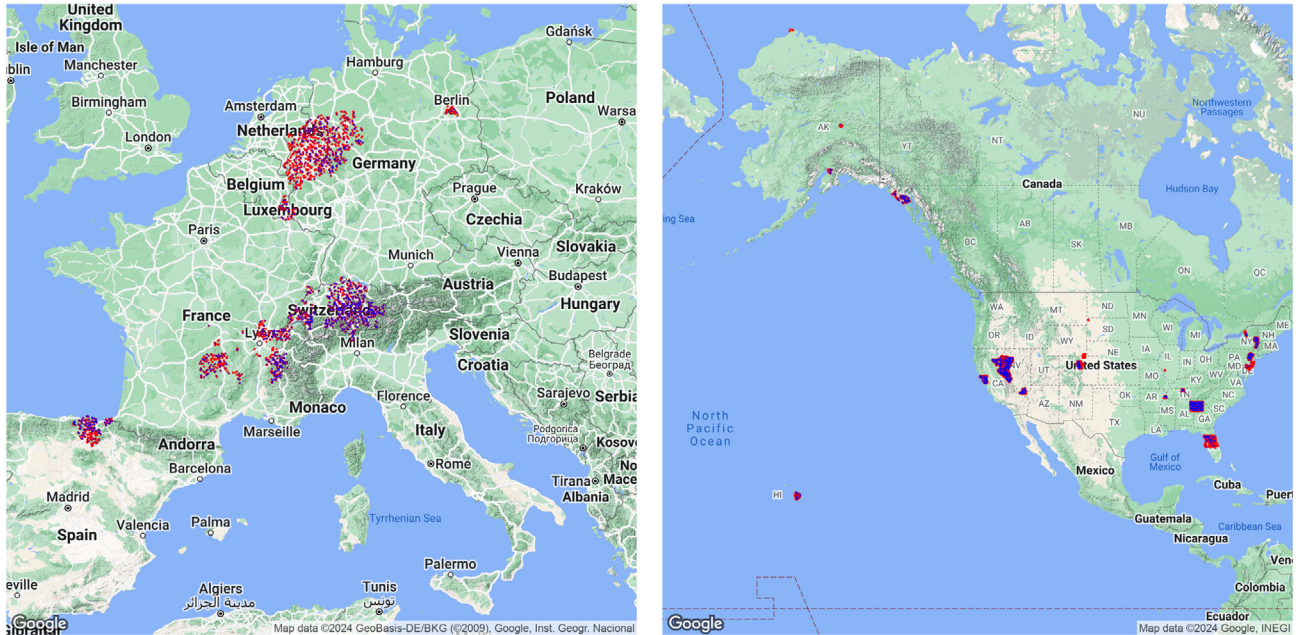


Figure 9. The map of Europe (left) and USA (right) with red dots indicating 52×10^6 uniformly sampled locations throughout the available data. The blue points indicate locations, where relative irradiation computed using 100 m maximum sampled topography deviates from reference by more than 10% (see Sections 3.2). The data from the USA constitutes 65% of all available data. Europe and America are shown with different scales.

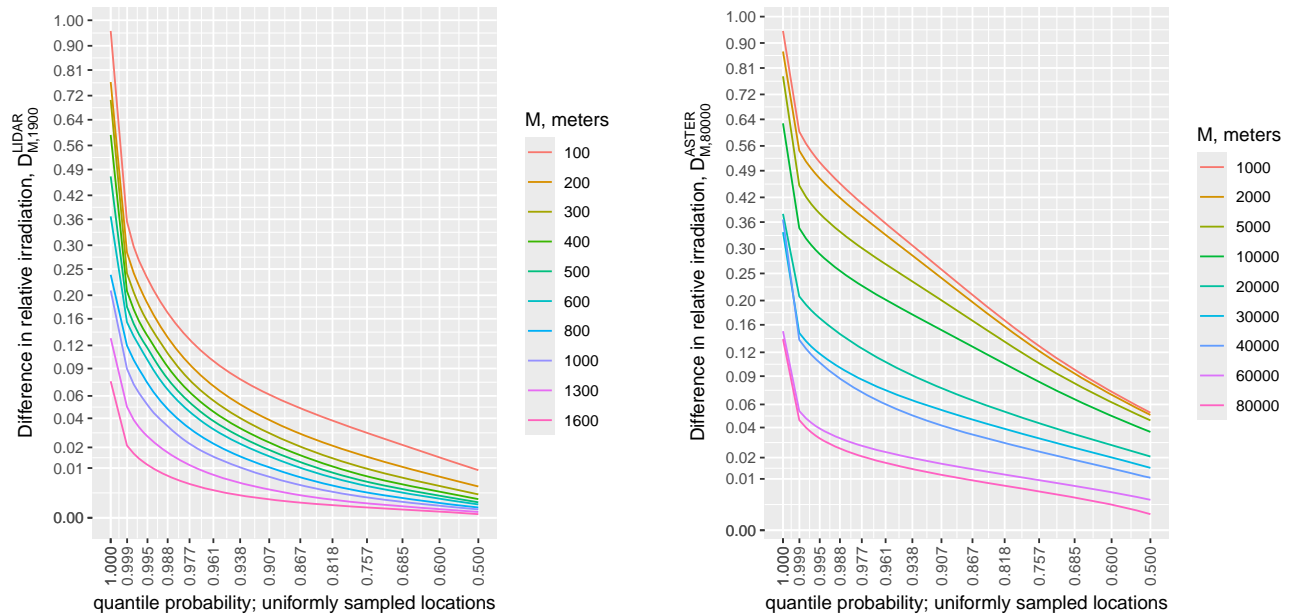


Figure 10. Right tail of the distribution of $D_{M,1.9\text{km}}^{\text{LIDAR}}$ (left) and $D_{M,120\text{km}}^{\text{ASTER}}$ (right). Note the nonlinear scaling of the axes.

4.7. Concluding Recommendation

We conclude that one must consider maximum sampled topography with care. In specific locations, the irradiation can be significantly overestimated for $M = 100$ m. In areas with

hills and mountains, one must combine sampling high-resolution topography at shorter distances (200 m) with large-resolution topography at more considerable distances (30 km). Tail distributions in Figure 10 provide an error rate for various distances.

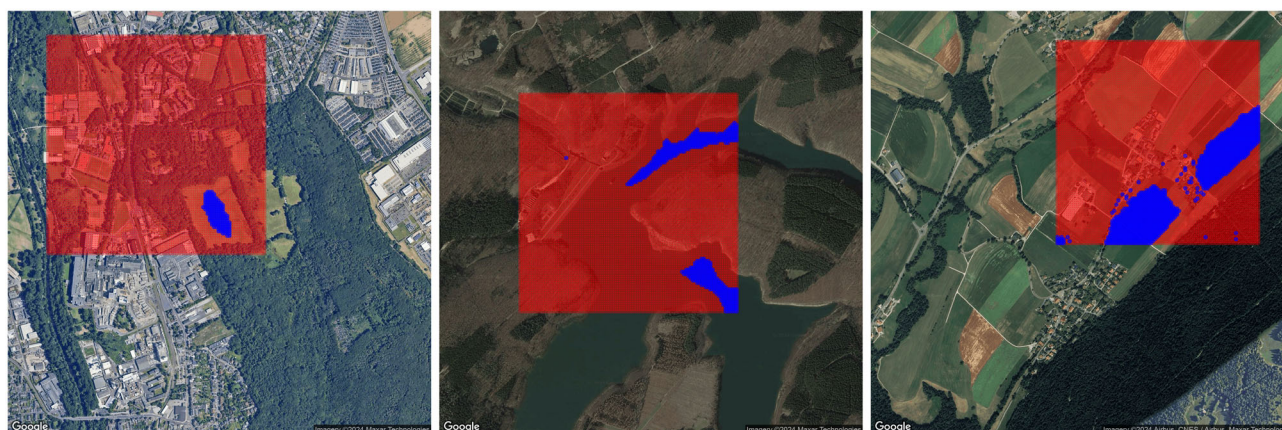


Figure 11. Red: sampled location. Blue: locations where $D_{\text{LIDAR}}^{100\text{m},1.9\text{km}} > 0.1$. Left: Düren, Germany. Center: Hürtgenwald, Germany. Right: next to the Chaumont ridge, Switzerland.

5. Concluding Discussion and Future Work

This study has evaluated the performance of several horizon approximation algorithms for VIPV and BIPV applications. We assessed the impact of the observer orientation on the curved-shaped commercial vehicle and elevation above the ground for facade points on the buildings in several cities in Germany. The errors between considered methods, while slightly varying with observer orientation, tend to increase with elevation. Hence, for instance, previously proposed approximate algorithms have similar accuracy and performance ratios on higher elevations for applications in roof irradiation.

Using a random search, we established the critical locations where maximum sampling distance matters most. The right tail of the error distribution provides practical advice on the maximum sampled distance. For accurate irradiation modeling, our recommendation is to have detailed topography data within a 200 m radius of the PV installation site and a broader view of the terrain within a 30 km radius.

Our findings bear significant implications for the field, offering practical insights into the most effective ways to model irradiation for PV solar potential. This contribution is not just theoretical, but it also paves the way for developing more efficient and accurate PV simulation tools. Computation speed improvements allow scaling up irradiation simulations for various integrated PV applications, making our research directly applicable in real-world scenarios.

The proposed family of horizon algorithms is implemented in our open-source irradiance modeling tool SSDP.^[29] The code and data generated for this article are published in ref. [43].

Acknowledgements

The authors gratefully acknowledge the Helmholtz Data Federation (HDF) for funding this work by providing services and computing time on the HDF Cloud cluster at the Jülich Supercomputing Centre (JSC). Furthermore, the authors gratefully acknowledge the Gauss Centre for Supercomputing e.V. (www.gauss-centre.eu) for funding this project by providing computing time through the John von Neumann Institute for Computing (NIC) on the GCS Supercomputer JUWELS at Jülich

Supercomputing Centre (JSC). This work was supported by the HGF project “Living Lab Energy Campus (LLEC)”, as well as the “Street” project (Street — Einsatz von hocheffizienten Solarzellen in elektrisch betriebenen Nutzfahrzeugen, Förderkennzeichen: 0324275A).

Open Access funding enabled and organized by Projekt DEAL.

Conflict of Interest

The authors declare no conflict of interest.

Author Contributions

Evgenii Sovetkin: Conceptualization (lead); Software (equal); Writing—original draft (lead); Writing—review & editing (equal). **Andreas Gerber:** Funding acquisition (lead). **Bart E. Pieters:** Software (equal); Writing—review & editing (equal).

Data Availability Statement

Data and scripts are available at: <https://doi.org/10.6084/m9.figshare.26114461>.

Keywords

horizons, sky-view factors, solar irradiance simulations

Received: June 30, 2024

Revised: August 21, 2024

Published online: September 19, 2024

- [1] E. Sovetkin, A. Gerber, B. E. Pieters, *Prog. Photovoltaics* **2024**, under review, <https://doi.org/10.22541/au.172114508.82017107/v1>.
- [2] M. C. Brito, R. Amaro e Silva, D. Pera, I. Costa, D. Boutov, *Prog. Photovoltaics* **2024**, 32, 73.
- [3] F. Karoui, F. Claudon, B. Chambion, S. Catellani, B. Commault, *J. Phys.: Conf. Ser.* **2023**, 2454, 012007.
- [4] H. Samadi, G. Ala, V. L. Brano, P. Romano, F. Viola, *World Electr. Veh. J.* **2023**, 14, 154.

- [5] E. Sovetkin, J. Noll, N. Patel, A. Gerber, B. E. Pieters, *Sol. RRL* **2023**, 7, 2200593.
- [6] N. Patel, R. Peibst, B. E. Pieters, E. Sovetkin, A. Reinders, *Prog. Photovoltaics* **2024**, under review, <https://doi.org/10.22541/au.171562054.49126865/v1>.
- [7] K. Araki, Y. Ota, M. Yamaguchi, *Appl. Sci.* **2020**, 10, 3.
- [8] Y. Zhou, M. Verkou, M. Zeman, H. Ziar, O. Isabella, *Sol. RRL* **2022**, 6, 2100478.
- [9] C. Ferri, H. Ziar, T. T. Nguyen, H. van Lint, M. Zeman, O. Isabella, *Renewable Energy* **2022**, 182, 427.
- [10] S. Bhattacharya, C. Braun, U. Leopold, *ISPRS Int. J. Geo-Inf.* **2021**, 10, 583.
- [11] B. Cabral, N. Max, R. Springmeyer, in *Proc. of the 14th Annual Conf. on Computer Graphics and Interactive Techniques*, New York, July **1987**, pp. 273–281.
- [12] N. L. Max, *Visual Comput.* **1988**, 4, 109.
- [13] E. Sovetkin, A. Gerber, B. E. Pieters, *Int. J. Geogr. Inf. Sci.* **2024**, under blinded review.
- [14] AIST, Japan Spacesystems, and US/Japan ASTER Science Team, 2009: ASTER Global Digital Elevation Model. NASA EOSDIS Land Processes DAAC, NASA, METI, cmr.earthdata.nasa.gov/search/concepts/C1711961296-LPCLOUD.html (accessed: September 2024).
- [15] Copernicus open Access Hub, scihub.copernicus.eu (accessed: September 2024).
- [16] R. Perez, R. Seals, J. Michalsky, *Sol. Energy* **1993**, 50, 235.
- [17] OpenStreetMap Contributors, OpenStreetMap: Map Data for Thousands of Websites, Mobile Apps, and Hardware Devices, <https://openstreetmap.org> (accessed: September 2024).
- [18] Openstreetmap Data Extracts, <https://download.geofabrik.de/> (accessed: September 2024).
- [19] 3D-Building Data in North Rhine-Westphalia, bezreg-koeln.nrw.de/geobasis-nrw/produkte-und-dienste/3d-gebaeudemodelle (accessed: May 2023).
- [20] Photovoltaic Geographical Information System PVGIS, joint-research-centre.ec.europa.eu/photovoltaic-geographical-information-system-pvgis/pvgis-tools/horizon-profile_en.
- [21] W. F. Holmgren, C. W. Hansen, M. A. Mikofski, *J. Open Source Software* **2018**, 3, 884.
- [22] Die Planungs- und Simulationssoftware für Photovoltaik-Systeme, valentin-software.com/produkte/pvsol/ (accessed: September 2024).
- [23] PVsyst: A Full Package for the Study of Your Photovoltaic Systems, pvsyst.com/ (accessed: September 2024).
- [24] M. Neteler, H. Mitasova, *Open Source GIS: A GRASS GIS Approach*, Springer, New York, NY **2013**.
- [25] Modeling Solar Radiation, pro.arcgis.com/en/pro-app/latest/tool-reference/spatial-analyst/modeling-solar-radiation.htm (accessed: September 2024).
- [26] O. Conrad, B. Bechtel, M. Bock, H. Dietrich, E. Fischer, L. Gerlitz, J. Wehberg, V. Wichmann, J. Böhrner, *Geosci. Model Dev.* **2015**, 8, 1991.
- [27] M. Keijzer, Master's Thesis, Delft University of Technology **2019**, resolver.tudelft.nl/uuid:d1a6baf0-7721-441e-bc2c-3a05bdaea89d (accessed: September 2024).
- [28] C. R. Steger, B. Steger, C. Schär, *Geosci. Model Dev.* **2022**, 15, 6817.
- [29] B. Pieters, E. Sovetkin, M. Gordon, SSDP: Simple Sky Dome Projector, github.com/IEK-5/SSDP (accessed: September 2024).
- [30] K. Zakšek, K. Oštir, Ž. Kokalj, *Remote Sens.* **2011**, 3, 398.
- [31] Z.-H. Jiao, H. Ren, X. Mu, J. Zhao, T. Wang, J. Dong, *Earth Space Sci.* **2019**, 6, 222.
- [32] D. Pera, C. Braun, P. Pinheiro, U. Leopold, in *Proc. of the 40th European Photovoltaic Solar Energy Conf. and Exhibition* **2023**, pp. 020322–001–020322–004.
- [33] A. V. Vo, D. F. Laefer, A. Smolic, S. I. Zolanvari, *ISPRS J. Photogramm. Remote Sens.* **2019**, 155, 119.
- [34] Á. Bognár, R. C. Loonen, J. L. Hensen, in *Proc. of Building Simulation 2021: 17th Conf. of IBPSA*, volume 17 of Building Simulation, IBPSA, Bruges, Belgium, ISBN 978-1-7750520-2-9, ISSN 2522-2708, September **2021**, pp. 1529–1536.
- [35] G. Agugiaro, F. Nex, F. Remondino, R. De Filippi, S. Droghetti, C. Furlanello, *ISPRS Ann. Photogramm. Remote Sens. Spatial Inf. Sci.* **2012**, 1, 177.
- [36] D. de Jong, H. Ziar, *Sol. RRL* **2023**, 7, 2200642.
- [37] D. Palmer, E. Koumpli, I. Cole, R. Gottschalg, T. Betts, *Energies* **2018**, 11, 3506.
- [38] M. C. Brito, P. Redweik, C. Catita, S. Freitas, M. Santos, *Energies* **2019**, 12, 3457.
- [39] F. Mansouri Kouhestani, J. Byrne, D. Johnson, L. Spencer, P. Hazendonk, B. Brown, *Int. J. Energy Environ. Eng.* **2019**, 10, 13.
- [40] D. A. Mira, M. Bartholomäus, S. Poessl, T. Kari Hass, P. Behrendorff Poulsen, G. Alves dos Reis Benatto, S. V. Spataru, in *Proc. of the 39th World Photovoltaic Solar Energy Conf. and Exhibition* **2022**, pp. 1304–1310.
- [41] J. M. Rodríguez, R. Herrero, L. San José, R. Núñez, I. A. Hernández, in *Proc. of the 40th European Photovoltaic Solar Energy Conf. and Exhibition* **2023**, pp. 020321–001–020321–005.
- [42] L. Morino, M. Bartholomäus, S. V. Spataru, P. B. Poulsen, in *Proc. of the 40th European Photovoltaic Solar Energy Conf. and Exhibition* **2023**, pp. 020324–001–020324–013.
- [43] E. Sovetkin, B. Pieters, M. Gordon, Data and Scripts for Reproducing Results in Paper Fast Horizon Approximation: Impacts on Integrated Photovoltaics Irradiation Simulations **2024**, <https://doi.org/10.6084/m9.figshare.26114461>.
- [44] US, Department of the Interior (DOI), RockyWeb: LIDAR Measurements, rockyweb.usgs.gov/vdelivery/Datasets/Staged/Elevation/LPC/Projects/ (accessed: September 2024).
- [45] 3D-Measurement Data in North Rhine-Westphalia, bezreg-koeln.nrw.de/brk_internet/geobasis/hoehenmodelle/3d-messdaten/index.html (accessed: May 2023).
- [46] Berlin, LIDAR data, fbinter.stadt-berlin.de/fb/berlin/service_intern.jsp?id=a_lod2@senstadttype=FEED (accessed: May 2023).
- [47] LIDAR 2019 - relevé 3d du territoire luxembourgeois, data.public.lu/fr/datasets/lidar-2019-releve-3d-du-territoire-luxembourgeois (accessed: September 2024).
- [48] Federal Office of Topography swisstopo, swisstopo.admin.ch/en/knowledge-facts/geoinformation/lidar-data.html (accessed: May 2023).
- [49] Accédez aux données open data du craig, drive.opendata.craig.fr/s/opendata (accessed: September 2024).
- [50] Ficheros binarios del vuelo LIDAR 2017 de la comunidad autónoma del país vasco, [ftp://ftp.geo.euskadi.eus/lidar/](https://ftp.geo.euskadi.eus/lidar/) (accessed: May 2023).